Molecular simulations of cement based materials: A comparison between first principles and classical force field calculations

Sylvia M. Mutisya [a], James M. de Almeida [a], Caetano R. Miranda [b],*

[a] CCNH, Universidade Federal do ABC, Santo André, SP 09210-580, Brazil
[b] DFMT, Instituto de Física, Universidade de São Paulo, São Paulo, SP 05508-090, Brazil

ABSTRACT

The heterogeneity and complexity of the cement structure and processes makes the interpretation of experimental data challenging. Atomistic simulations allow investigations at the atomic level of interactions, thus having the potential to provide complementary information to experiments. In this regard, the investigation of the transferability of the available force fields as well their ability to predict the properties of interest is an important prerequisite. In this work, we compare CLAYFF force field against first principles Density Functional Theory (DFT) calculations focusing on its ability to predict structural, vibrational and thermodynamic properties of cement phases differing in the degree of hydration. The systems studied include tobermorite 9 Å, 11 Å, 14 Å, gypsum, tricalcium aluminate and ettringite. Our results indicate that CLAYFF describes well the lattice parameters within acceptable errors. However for the vibrational properties, there is a significant alteration in the silicate, sulfate, water and OH frequencies in comparison to DFT and experimental results. DFT Bader charge analysis indicate that the charge on the interlayer calcium ions in tobermorite does not change with increase in hydration, implying that the nature inter-atomic bonding within the layers remain unchanged. For the thermodynamic quantities investigated (*i.e.* Helmholtz free energy, entropy and specific heat), CLAYFF results are in agreement with DFT calculations. Our findings indicate that water enhances the stability of the hydrated phases based on the lower values of the Helmholtz free energy. We demonstrate that CLAYFF can capture consistently the thermodynamic properties of cement phases.

© 2017 Elsevier B.V. All rights reserved.

1. Introduction

Cement is one of the most consumed material in the world and its manufacturing process is responsible for about 8% of the total world CO_2 emissions [1,2]. Most of the cement produced is used to prepare concrete in addition to other applications such as a barrier for nuclear wastes [3,4] and for solidification/stabilization of a broad range of contaminated materials [5]. To improve the durability of concrete structures as well as produce novel cements for applications in extreme environments, it is important to understand the structure and thermodynamic properties of cement at a molecular level.

One of the major challenges in cement science is the limited understanding of the structure of the main hydration phase, calcium silicate hydrate ($CaO·SiO_2·H_2O$ or C-S-H) [6]. C-S-H is known to be poorly crystalline to almost amorphous material, with structure organized over sizes less than 100 Å [7]. It has a complex pore structure spanning over tens and hundreds of nanometers [8–10]. Nanoindentation analysis by Constantinides et al. [11] have shown that mechanically, C-S-H behaves as a nanogranular material composed of two distinct densities. A recent study has unveiled an extended pore network and a continuum distribution of local densities [12] beyond the colloid model [13,14] based on two distinct local densities. The atomic structure of C-S-H is not yet fully described, but XRD experiments have showed its similarities with the naturally occurring crystalline mineral, tobermorite [15–17].

Although C-S-H is associated with most of the properties observed in cement, other hydrated cement phases play a role in durability. One such phase is ettringite ($Ca_6[Al(OH)_6]_2·[SO_4]_3·26H_2O$) which is produced from the hydration of tricalcium aluminate ($3CaO·Al_2O_3$ or C_3A) in the presence of gypsum ($CaSO_4·2H_2O$). The chemical reaction of C_3A and gypsum is shown in Eq. (1).

$$Ca_3Al_2O_6 + 3(CaSO_4 \cdot 2H_2O) + 26H_2O$$
$$\rightarrow Ca_6[Al(OH)_6]_2 \, [SO_4]_3 \cdot 26H_2O \tag{1}$$
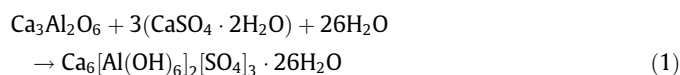
* Corresponding author.
  E-mail address: cmiranda@if.usp.br (C.R. Miranda).

Ettringite formation both controls the kinetics of hardening as well as maintains a good workability at early ages [18]. On the other hand, the presence of ettringite in mature cement paste is associated with degradation of concrete structures [19–21]. Delayed ettringite formation can be due to the availability of sulfate [22,23] or if the concrete mixture is under steam curing conditions with subsequent moist conditions [24]. It is believed that the formation of ettringite is a volume expanding reaction which causes damage to the cement paste [25,26]. However, the damage caused by sulfate attack cannot be explained solely by ettringite precipitation, and the link between ettringite formation and expansion is not clear [27,28].

The complexity of the cement structure and the processes responsible for the observable properties makes the interpretation of experimental data challenging. Atomistic simulations have the potential to provide useful information on understanding the structure of materials, since they allow investigations at the atomic level of interactions. Since the accuracy of atomic simulations is dependent on the choice of force field, detailed tests of the force field's description of the properties of interest is necessary.

A number of force fields have been optimized for cementitious materials including CSH-FF [29], INTERFACE [30] and REAXFF [31] force fields. In this work, we focus on CLAYFF [32] which was tested on a variety of systems including boehmite, portlandite, kaolinite, pyrophylite, montmorillonite and hydrotalcite. In CLAYFF formulation, most interatomic interactions are treated as non-bonded. This allows the force field to be used for a wide variety of phases and to properly account for energy and momentum transfer between the fluid phase and the solid, while keeping the number of parameters small enough to allow modeling of relatively large and highly disordered systems. Over the years, CLAYFF force field has been used widely in the study of clays [33–35] and cement materials [36–38]. In this study, we investigate CLAYFF's accuracy in the description of structural, vibrational and thermodynamic properties for hydrated and anhydrous cement phases. Of interest here is the main hydration phase (C-S-H) which is responsible for the majority of the cement mechanical properties and the hydration reaction which produces ettringite due to its link to concrete deterioration. We model the C-S-H atomic structure with tobermorite crystal and in this regard, we investigated three phases of tobermorite (tobermorite 9 Å, 11 Å and 14 Å) which differ in the degree of hydration. In relation to the ettringite formation, we studied gypsum, tricalcium aluminate and ettringite.

Investigation of the vibrational frequencies reveals the stability of the relaxed systems and the frequencies can be directly compared to infrared and Raman spectra experiments. In addition, thermodynamic properties are useful in establishing stability relationships in terms of fluid composition, temperature and pressure. Experimentally, this ability is limited due to uncertainties in the quality of data especially for cementitious materials. Experimental data obtained by different approaches such as calorimetry, phase equilibria and solubility experiments is often conflicting due to problems intrinsic to the methods employed. Some sources of thermodynamic experimental data of cement phases include the compilations by Sarker et al. [39], Glasser et al. [40] and Taylor [41]. On the other hand, theoretical investigation of thermodynamic properties of minerals is challenging because it involves the comparison of anhydrous mineral which is governed by ionic and covalent interactions with a molecular liquid or crystal depending on the water reference state which may involve many interactions. Few theoretical studies have been conducted on the thermal properties of cement [42–44], thus verifying the performance of classical force fields in the description of these properties is important for future investigations.

2. Computational details

2.1. First principles calculations

First principles calculations were performed within the Density Functional Theory (DFT) [45,46] using the plane-wave basis projector augmented wave method [47] and the generalized gradient approximation in the Perdew-Burke-Ernzerhof [48] as implemented in the Vienna Ab-initio Simulation Package (VASP) [49,50] simulation package. After thorough convergence tests, the plane wave energy cutoff was found to be 450 eV. Initial configurations of all the structures were obtained from experimental data and then the unit cell parameters and atomic positions optimized with a force convergence criterion of 10^{-4} eV/Å. Atomic charges on all atoms were obtained by performing a Bader analysis on the charge density calculated from VASP using the Bader analysis code by Henkelman et al. [51].

2.2. Molecular mechanics calculations

Classical molecular mechanics (MM) simulations were performed using LAMMPS [52] simulation package. The ion–ion, water–water and ion–water interactions were described using the CLAYFF [32] force field. The bonded interaction parameters describing the bond stretching and angle bending of the sulfate anion in gypsum and ettringite were adopted from the work by Kalinichev et al. [53]. Long range coulombic interactions are calculated using the PPPM method [54] with a cut-off radius of 10 Å. The search for local minima followed the conjugate gradient [55] procedure. More strict convergence criterion was applied for tobermorite 11 Å, tobermorite 14 Å and ettringite due to the large number of water molecules and OH groups.

2.3. Phonon calculations

The minimized structures from both first principles and classical MM simulations were used as input for the phonon calculations. The finite difference method using the Phonopy code [56] with a uniform displacement of 0.01 Å was used for the calculation of the harmonic vibrational frequencies. The phonon spectrum was computed by using supercells of $2 \times 2 \times 2$ for tobermorite 9 Å, tobermorite 11 Å, tobermorite 14 Å and gypsum. The $2 \times 2 \times 2$ supercells were not optimized because the sizes of the unitcells are relatively large, thus we do not expect a considerable change of the properties of interest after replication. The C_3A and ettringite unit cells did not need to be replicated, as the unit cells are already large enough to avoid spurious interactions with neighboring cells. During the forces calculation by both first principles or MM techniques, the cell volume and atomic positions were fixed. A major challenge in the calculation of phonons using first principles approach in these systems is the high computational cost because of the large supercell sizes.

The thermodynamic quantities (Helmholtz free energy (F), specific heat at constant volume (C_v) and entropy (S)) were obtained from the phonon frequencies by the following relations:

$$F = \sum_{\mathbf{q}j} \left[\frac{1}{2}\hbar\omega_{\mathbf{q}j} + k_B T \ln[1 - \exp(-\hbar\omega_{\mathbf{q}j}/k_B T)] \right] \quad (2)$$

$$C_v = \sum_{\mathbf{q}j} k_B \left(\frac{\hbar\omega_{\mathbf{q}j}}{k_B T} \right)^2 \frac{\exp(\hbar\omega_{\mathbf{q}j}/k_B T)}{[\exp(\hbar\omega_{\mathbf{q}j}/k_B T) - 1]^2} \quad (3)$$

$$S = \frac{1}{2T}\sum_{\mathbf{q}j} \hbar\omega_{\mathbf{q}j} \coth[\hbar\omega_{\mathbf{q}j}/2k_B T] - k_B \sum_{\mathbf{q}j} \ln[2\sinh(\hbar\omega_{\mathbf{q}j}/2k_B T)] \quad (4)$$

where k_B, T, $\omega_{\mathbf{q}j}$ and $\hbar$ is the Boltzmann constant, temperature, the j_{th} phonon frequency and the reduced Planck's constant respectively. All thermodynamic properties were calculated at constant volume within the harmonic approximation.

3. Results and discussion

3.1. Structural properties

3.1.1. Tobermorites

Tobermorites are calcium silicate hydrate minerals characterized by CaO layers parallel to the (001) plane. The CaO layers are connected by wollastonite-like silicate chains on both sides (see Fig. 1). Depending on the degree of hydration, the basal spacing can be either 9 Å, 11 Å or 14 Å corresponding to tobermorite 9 Å ($Ca_5Si_6O_{16}(OH)_2$), tobermorite 11 Å ($Ca_{4.5}Si_6O_{16}(OH)\cdot5H_2O$) and tobermorite 14 Å ($Ca_5Si_6O_{16}(OH)_2\cdot7H_2O$) [57–59] respectively. By heating tobermorite 14 Å, it transforms to normal tobermorite 11 Å at 353 K then subsequently to tobermorite 9 Å at 553 K [60]. In this study, the models for tobermorite 9 Å and normal tobermorite 11 Å are the triclinic polytype by Merlino et al. [57] and the monoclinic polytype MDO$_2$ by Merlino et al. [58] respectively. The structure for tobermorite 14 Å is the monoclinic polytype MDO$_2$, space group B11b by Bonaccorsi et al. [59].

The optimal lattice parameters in comparison to experiment and other simulations are shown in Table 1. Both first principles and MM simulations reproduce the lattice parameters within 3.5 % of experiments. For the tobermorite 9 Å, all the parameters calculated from first principles are greater than the experimental values, with this observed only for a and b axes in tobermorite 11 Å and c axis in tobermorite 14 Å. The overestimation of lattice parameters in the tobermorite 9 Å structure is in line with the typical performance of GGA approximation, which tends to overestimate bond lengths and cell vectors in solids [61]. The shorter c vector in tobermorite 11 Å and b vector in tobermorite 14 Å from first principles

simulations was also obtained in Vidmer et al. [62] work. Si—O bond length varies from 1.58 to 1.69 Å and 1.54 to 1.62 Å for first principles and MM simulations respectively. The experimental values for the Si—O bond lengths in tobermorite structures ranges from 1.56 to 1.74 Å [57–59]. While there is a slight increase of the Si—O bond distances from first principles simulations, CLAYFF underestimates these bond distances in comparison to experiments which may explain the shorter cell vectors over all the tobermorite systems.

3.1.2. Tricalcium aluminate, gypsum and ettringite

The structure of C$_3$A consists of hollow rings of six corner sharing AlO$_4$ tetrahedra held together by Ca ions (Fig. 2 b)). There are two distinguishable Al sites, one with aluminum atoms having a regular octahedral environment while the other has a planar coordination [63]. The C$_3$A structure by Mondal et al. [64] was used in our calculations. The lattice constants determined from both first principles and MM approaches are in good agreement with the experiments as shown in Table 1. The mean bond distances for the Al—O atoms forming the rings range from 1.73 to 1.77 Å and 1.75 to 1.79 Å for first principles and MM simulations respectively. The average Al—O bond length from X-ray data is 1.75 Å [64]. The Al—O bond distance calculated from first principles and MM simulations compare well with both experiment and other simulations [65].

Gypsum, on the other hand, contains both molecular water and sulfate groups ionically bound to calcium polyhedra [66] (Fig. 2a)). The chosen unit cell in this study is that selected by Comodi et al. [66] with space group C2/a. The symmetry of the cell is preserved after relaxation in both approaches. The lattice parameters are slightly overestimated (see Table 1) from first principles simulations, attributed to GGA approximation. The sulfate anion, described by a harmonic interaction in CLAYFF force field is symmetric with an average S—O bond distance of 1.48 Å while from first principles calculations its asymmetric, with two distinct S—O bond lengths of either 1.49 Å or 1.50 Å. In gypsum, the average S—O bond distance obtained from X-ray experiments is 1.4733 Å [66]. CLAYFF indicate a better agreement with this value in relation to DFT calculations. Examining the O—S—O angles, we found that the sulfate anion from MM simulations has angles ranging from 108° to 110° in relation to first principles simulations with O—S—O angle being either 106.22° or 111.25°.

Ettringite forms hexagonal, elongated prismatic crystals consisting of columns of Ca$_3$[Al(OH)$_6$·12H2O]$^{3+}$ lying parallel to the c-axis with water and sulfate in the inter-column channels [67] as shown in Fig. 2c). Aluminum atoms are sixfold coordinated with hydroxyls while the calcium atoms are each eightfold coordinated with four hydroxyls and four water molecules. The structure for ettringite used in this study is by Hartman et al. [68]. Similar to other hydrated phases investigated here, CLAYFF force field also underestimates the lattice constants in ettringite. Other molecular mechanics simulations using CLAYFF [53] agree with our findings. The bond distances of Al—O range between 1.91 and 1.92 Å and 1.91 and 1.98 Å for first principles and MM simulations respectively. Sulfate anions in ettringite structure are in a more complex environment in comparison to gypsum, thus, it is expected a larger variation of the S—O bond distances and O—S—O angles. S—O bond distances range from 1.44 to 1.49 Å for first principles calculations, while from MM simulations, this value is 1.47 Å for all bonds. Experimental S—O bond length in ettringite is 1.49 Å [68], indicating a slight underestimation of these parameters by both our DFT and MM simulations.

3.2. Electronic structure analysis

To have more insight on the electronic structure and interatomic bonding characteristics, we performed a Bader analysis
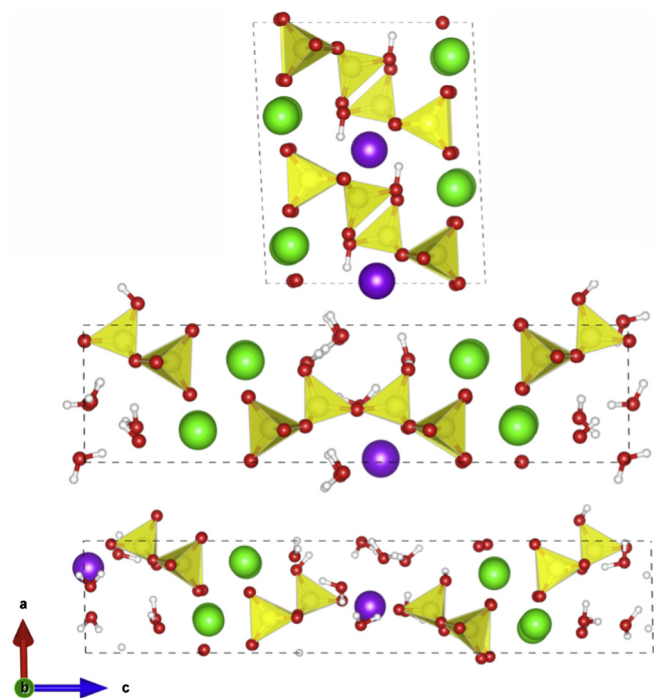
Fig. 1. Atomic structures of (a) tobermorite 9 Å [57], (b) tobermorite 11 Å [58] and (c) tobermorite 14 Å [59] in the (010) plane. Color legend: O, red; H, white; Ca within layers, green; Interlayer Ca, purple; Si, yellow polyhedra. (For interpretation of the references to colour in this figure legend, the reader is referred to the web version of this article.)

Table 1
Simulated CLAYFF and 0 K DFT lattice parameters for tobermorite 9 Å, 11 Å, 14 Å, ettringite, C$_3$A and gypsum in comparison to other simulations and experimental data (at ambient conditions).

System		Lattice parameters					
		a (Å)	b(Å)	c(Å)	α (deg)	β (deg)	γ (deg)
Tobermorite 9 Å	This work, first principles	11.19	7.39	9.70	100.82	92.69	90.07
	This work, MM	11.15	7.29	9.55	101.08	92.83	89.98
	DFT-GGA [69]	11.20	7.41	9.71	100.9	93.10	90.10
	CLAYFF [53]	11.16	7.26	9.61	103.47	89.46	90.13
	Expt [57]	11.16	7.30	9.57	101.08	92.83	89.98
Tobermorite 11 Å	This work, first principles	6.81	7.46	22.65	89.91	90.47	122.93
	This work, MM	6.71	7.35	22.62	90.00	90.00	123.18
	DFT-GGA [62]	6.82	7.46	22.67	90.27	89.12	123.24
	CSH-FF [29]	6.6	7.39	24.37	90.0	90.0	123.88
	Expt [58]	6.73	7.37	22.68	90.00	90.00	123.18
Tobermorite 14 Å	This work, first principles	6.74	7.42	28.40	90.54	90.71	123.46
	This work, MM	6.69	7.19	27.84	90.00	90.00	123.25
	DFT-GGA [62]	6.64	7.14	28.18	90.00	89.99	121.66
	COMPASS [70]	6.64	7.31	27.57	90.00	90.00	123.25
	CSH-FF [29]	6.70	7.41	28.70	90.01	89.81	123.77
	Expt [59]	6.74	7.43	27.99	90.00	90.00	123.25
Ettringite	This work, first principles	11.17	11.17	21.35	90.00	90.00	120.00
	This work, MM	10.96	10.96	20.95	90.00	90.00	120.00
	DFT-GGA [71]	11.22	11.22	21.87	90.00	90.00	120.00
	CLAYFF [53]	11.02	10.94	21.30	90.50	89.80	119.80
	REAXFF [31]	11.53	11.53	22.22	90.50	89.80	119.80
	Expt [68]	11.17	11.17	21.35	90.00	90.00	120.00
Tricalcium Aluminate	This work, first principles	15.26	15.26	15.26	89.99	89.99	90.00
	This work, MM	15.26	15.26	15.26	90.00	90.00	90.00
	DFT-GGA [72]	15.38	15.38	15.38	90.00	90.00	90.00
	INTERFACE [65]	15.27	15.26	15.26	90.00	90.00	90.00
	Expt [64]	15.26	15.26	15.26	90.00	90.00	90.00
Gypsum	This work, first principles	6.40	15.17	5.72	90.00	114.35	90.00
	This work, MM	6.26	15.13	5.65	90.00	114.11	90.00
	Expt [66]	6.28	15.18	5.67	90.00	114.11	90.00
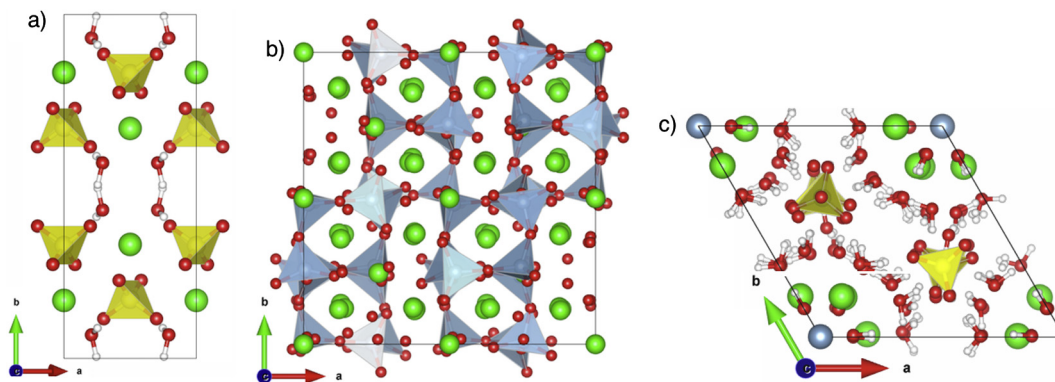
Fig. 2. Atomic structures of (a) gypsum, [66] (b) tricalcium aluminate [64] and (c) ettringite [67]. Color legend: O, red; H, white; Ca, green; Al, blue polyhedra; S, yellow polyhedra. (For interpretation of the references to colour in this figure legend, the reader is referred to the web version of this article.)

[51] of the charge density. For the MM simulations, the charges are fixed and this dictates the kind of bonding involved in the atomic interactions. Table 2 compares the charge on each atom species using the Bader analysis with the atom charges used in CLAYFF model. The partial atomic charges in CLAYFF model are assigned according to the Mulliken charge of electronic densities from DFT calculations of simple oxide, hydroxide, and oxyhydroxide model compounds with well defined structures [32]. Although the partial charges in CLAYFF model are obtained from DFT simulations, Table 2 shows that they are significantly different from our DFT calculations, implying that the overall coulombic energy is likely to be different. The significance of using the partial charges in CLAYFF is that the interactions are soft allowing more flexibility and atomic motion [32]. Charges from other classical force fields

optimized for cement materials have been included in Table 2 for comparison.

All the minerals in the tobermorite group are characterized by sevenfold coordinated Ca ions. These polyhedra are similar and from our analysis, the Ca ions have comparable net charges: +1.61 *e* for the tobermorite 9 Å and 14 Å and +1.62 *e* in tobermorite 11 Å. Within the structural interlayers, tobermorite 11 Å and 14 Å contains 'zeolitic' calcium ions and water molecules. The 'zeolitic' calcium ions in tobermorite 11 Å and 14 Å are coordinated to both oxygen from the silicates and water molecules [58,59]. In tobermorite 9 Å, all the water is lost and the 'zeolitic' Ca ions are linked to oxygen and hydroxyls [57]. These 'zeolitic' Ca ions here termed as interlayer calcium (see Fig. 1) have similar charges (+1.63 *e* and +1.64 *e*) despite increasing hydration from tobermorite 9 Å to 14 Å.

Table 2
Calculated atomic charges of different species obtained by Bader analysis compared with CLAYFF partial charges and other classical force fields.

System	Atom	Charge (e)			
		First principles	CLAYFF [32]	CSH-FF[29]	INTERFACE [30]
Tobermorite 9 Å	Calcium	1.61	1.05	1.435	1.5
	Interlayer calcium	1.64	1.05	1.706	1.5
	Silicon	3.13	2.1	1.722	1.0
	Bridging oxygen (silicate)	−1.62	−1.05	−1.01,−1.13	−0.5
	Terminal oxygen (silicate)	−1.56	−1.05	−1.15,−1.26	−1
	Interlayer oxygen (silicate)	−1.54	−1.05	−1.15,−1.26	−1
	Hydroxyl oxygen	−1.42 to −1.44	−0.95	−0.93,−0.97	−0.66
	Hydroxyl hydrogen	0.62 to 0.63	0.425	0.425	0.41
Tobermorite 11 Å	Calcium	1.62	1.05	1.435	1.5
	Interlayer calcium	1.63	1.05	1.706	1.5
	Silicon	3.14	2.1	1.722	1
	Bridging oxygen (silicate)	−1.59 to −1.61	−1.05	−1.01,−1.13	−0.5
	Terminal oxygen (silicate)	−1.56	−1.05	−1.15,−1.26	−0.925
	Interlayer oxygen (silicate)	−1.50, −1.54	−1.05	−1.15,−1.26	−0.925
	Hydroxyl oxygen	−1.46	−0.95	−0.93,−0.97	−0.66
	Water oxygen	−1.23 to −1.32	−0.82	−0.82	−0.82
	Hydroxyl hydrogen	0.65	0.425	0.425	0.41
	Water hydrogen	0.61 to 0.64	0.41	0.41	0.41
Tobermorite 14 Å	Calcium	1.61	1.05	1.435	1.5
	Interlayer calcium	1.64	1.05	1.706	1.5
	Silicon	3.14	2.1	1.722	1.0
	Bridging oxygen (silicate)	−1.61 to −1.62	−1.05	−1.01,−1.13	−0.5
	Terminal oxygen (silicate)	−1.56	−1.05	−1.15,−1.26	−1
	Interlayer oxygen (silicate)	−1.52	−1.05	−1.15,−1.26	−1
	Hydroxyl oxygen	−1.42 to −1.45	−0.95	−0.93,−0.97	−0.66
	Water oxygen	−1.22 to −1.30	−0.82	−0.82	−0.82
	Hydroxyl hydrogen	0.60 to 0.65	0.425	0.425	0.41
	Water hydrogen	0.59 to 0.66	0.41	0.41	0.41
Gypsum	Calcium	1.66	1.5 [73]		1.5
	Sulfur	3.84	0.5 [73]		0.5
	Oxygen (sulfate)	−1.37, −1.38	−0.5 [73]		-0.5
	Water oxygen	−1.27	−0.82		−0.82
	Water hydrogen	0.63	0.41		0.41
Tricalcium aluminate	Aluminum	2.43	1.575		1.2
	Calcium	1.52 to 1.56	1.05		1.5
	Oxygen	−1.56, −1.63	−1.05		−0.75, −1.35
Ettringite	Aluminum	2.47	1.575		1.2
	Calcium	1.63	1.36		1.6
	Oxygen (sulfate)	−1.31 to −1.36	−1.0		-0.6
	Sulfur	3.82, 3.80	2.0		0.6
	Oxygen	−1.39 to −1.42	−0.8675 [53]		−0.9
	Water oxygen	−1.24 to −1.31	−0.82		0.82
	Hydroxyl hydrogen	0.59 to 1.62	0.425		0.35
	Water hydrogen	0.62 to 0.65	0.41		0.41

This implies that the nature of the bonds between and within the layers remain unchanged. Pellenq et al. [74] showed that the interlayer Ca ions in tobermorite C—S—H model occupy specific crystallographic sites even after increasing the interlayer distance from 7.5 Å to 16 Å, indicating that those ions form a chemical bond with the oxygen atoms of the silicate. These charges for the interlayer Ca ions in tobermorite 11 Å and 14 Å are still far from that of an aqueous Ca ion (+2 *e*), an indication that the Ca ions are not fully hydrated. Among the force fields compared in Table 2, only CSH-FF has different charges for the two types of Ca ions in tobermorite phases.

From the charges obtained from DFT Bader analysis, other than the oxygens in water molecules and hydroxyl groups, the oxygen atoms in tobermorite can be grouped into bridging, terminal and interlayer oxygens all in the silicate chains. The bridging oxygens' charges varies from −1.59 *e* to −1.62 *e* which differs from the terminal oxygens whose charge is uniform (*i.e.* −1.56 *e*) in all the tobermorite systems. The oxygens termed as interlayer oxygen refer to the oxygen connected to the interlayer Ca ions. For tobermorite 9 Å, the interlayer oxygen refers to O6, O4, O1 and O11 (same notation as used by Merlino et al. [57]). Likewise, the inter-

layer oxygen refers to O6 and O5 [58,59] in tobermorite 11 Å and 14 Å respectively. For the case of tobermorite 11 Å, the interlayer calcium is located on either side (upper/lower) of the cavity, with water molecules located on the opposite. This implies that the O6 oxygens form bonds with interlayer calcium on one side and the other side with water molecules. We can see this bonding difference in the interlayer oxygen charges, where the O6 oxygen coordinated to interlayer calcium has a net charge of −1.54 *e* while for the O6 forming strong hydrogen bonds with water molecules the charge is −1.50 *e*. In tobermorite 14 Å, the O5 oxygen atoms are strongly bonded to interlayer Ca ions. In addition, they are also acceptors of a very strong hydrogen bond from one water molecule [59]. The atomic charge of the interlayer oxygen in tobermorite 14 Å from our calculations is −1.52 *e*, which is lower than the charges for the respective atoms in tobermorite 9 Å and 11 Å. The terminal and interlayer oxygen atoms have the same atomic charge in all the force fields compared in Table 2.

In gypsum and ettringite, the calcium ions are eightfold coordinated with two water molecules and six oxygens of the sulfate groups [66] in gypsum and with four hydroxyls and four water molecules in ettringite [68]. The atomic charges are equivalent in

the respective system, indicating that they all lie in the same chemical environment. On the other hand, in C_3A, the coordination of calcium ions is either octahedral or irregular with 5 or 6 oxygens [6]. We see this variation in the atomic charges ranging from +1.52 to +1.56 e (see Table 2).

The oxygen atoms in C_3A are separated into two groups with atomic charges -1.56 e and -1.63 e. This corresponds to ring and apical oxygens forming the Al_6O_{18} rings [65]. As shown in Table 2, the INTERFACE force field differentiates the two kinds of oxygen atoms, but in CLAYFF both have the same atomic charge. Upon hydration, these oxygens form aluminol and hydroxyl groups in ettringite. The atomic charges changes accordingly as shown in Table 2 for the oxygen atoms in ettringite. In gypsum, the oxygen atoms covalently bonded to sulfur are divided into two groups having atomic charges -1.37 e and -1.38 e. In contrast, the charges on the oxygen atoms varies from -1.31 e to -1.36 e in ettringite, which we attribute to the large amount of water molecules surrounding the sulfate anions. These findings indicate that the sulfate anion in gypsum and ettringite is asymmetric.

3.3. Vibrational density of states

Fig. 3 shows the total vibrational density of states of the tobermorite phases calculated from both first principles and MM approaches. The similarities in the vibrational density of states in the tobermorite phases confirm their structural resemblance. Although there is a lot of similarities between the three structures, they differ in important aspects relating to silicate polymerization, H_2O content and H_2O/OH environments [75]. To investigate how well classical MM and first principles calculations show the differ-

ent aspects, we plotted the contribution of each atomic species, shown in Fig. 4.

The Ca—O bond vibrations correspond to the frequencies in the range 0–450 cm^{-1} which is in agreement with other simulations [62] and infrared experiments [75]. Both classical MM and first principles approaches show good agreement for the Ca—O bond vibrations.

The frequencies associated with silicates range from 0 to 1200 cm^{-1} with experimental work by Yu et al. [75] showing that the frequencies at 400–500 cm^{-1} are associated with the deformation of SiO_4, while at around 660 cm^{-1}, they represent Si—O—Si bending vibrations and in the 800–1200 cm^{-1} range they correspond to the symmetric/asymmetric stretching of Si—O bonds.

From our calculations, the SiO_4 deformation frequencies predicted by MM simulations are localized and shifted to lower frequencies. These findings are in line with the short Si—O bonds observed in all the tobermorite phases. First principles calculations predict well the bending frequencies, [62,75] indicated by a sharp peak at around 650 cm^{-1} in all the systems. In contrast, in this frequency range, MM simulations show a broad range of frequencies from 500 to 800 cm^{-1}. For the symmetric/asymmetric stretching of Si—O bonds, we observe a shift to higher frequencies for all the tobermorite phases from classical MM calculations.

The vibrational frequencies around 1600 cm^{-1} seen only in tobermorite 11 Å and tobermorite 14 Å are due to the H—O—H bending of water molecules. These vibrations are absent in the tobermorite 9 Å since there are no water molecules in the structure. The bands of tobermorite 14 Å are stronger indicating more water in comparison to the tobermorite 11 Å structure. Both first principles and classical MM agree well in the prediction of these frequencies and compare well with experiment [75] (see Figs. 3 and 4).

The high frequency vibrations in the ranges 2900–3700 cm^{-1} are due to symmetric/asymmetric stretching of OH groups in water or hydroxyls with a variable range of hydrogen bond strength due to different environments. In the tobermorite 9 Å structure, the frequencies due to the hydroxyl groups show peaks at 3491 cm^{-1} and at 3668 cm^{-1} for the first principles and MM calculations respectively. The shifting to higher frequencies by classical MM calculations indicates that the force field describes the hydroxyls to be weakly hydrogen bonded. These range of frequency corresponds to a O···O of about 3.07 Å according to Novak A. correlation [76]. We relate this to the short Si—O bond lengths described by the CLAYFF, resulting to hydroxyls forming weak hydrogen bonds with the neighboring silicate oxygens.

First principles calculations for tobermorite 11 Å show peaks at 3104, 3318, 3435 and 3493 cm^{-1} due to water molecules and a peak at 3435 cm^{-1} due to hydroxyl groups. Ab-initio molecular dynamics calculations at about 300 K for normal tobermorite 11 Å by Churakov [77], showed an asymmetric spectrum with a maximum at 3640 cm^{-1} and a shoulder near 3400 cm^{-1}, with a small band at 3000 cm^{-1}. In our calculations, the band with a peak at 3493 cm^{-1} is attributed to the water which is not bound to the interlayer calcium, while highly hydrogen bonded water molecules have vibrational frequencies peaked at 3104 cm^{-1}. Experimental infrared spectrum for tobermorite 11 Å show major peaks at 3600 cm^{-1} and at 3300 cm^{-1} (Figs. 3 and 4). The weak peak at 3104 cm^{-1} observed in our DFT simulations is not present in experiments which may be attributed to strong background absorption. On the other hand, the frequencies obtained via MM simulations in the same frequency range show two peaks at around 3700 cm^{-1} corresponding to the symmetric and asymmetric stretching of water and hydroxyls.

Infrared studies of tobermorite 14 Å by Yu et al. [75] showed a strong and poorly resolved band in the ranges 2800–3700 cm^{-1} with a major maximum at 3480 cm^{-1} which is in agreement with
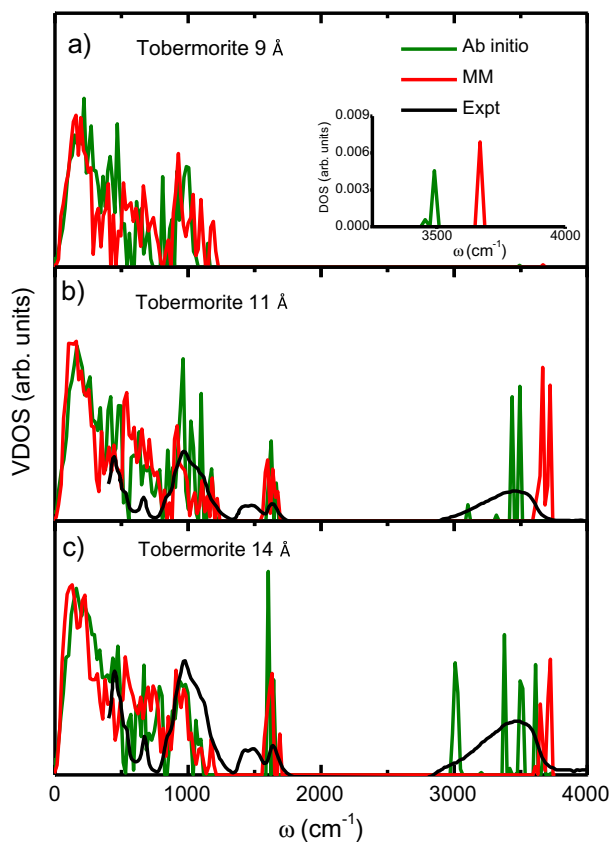
Fig. 3. Total vibrational density of states of the tobermorite phases calculated from first principles and classical MM approaches. The experimental infrared data is adapted from [75].
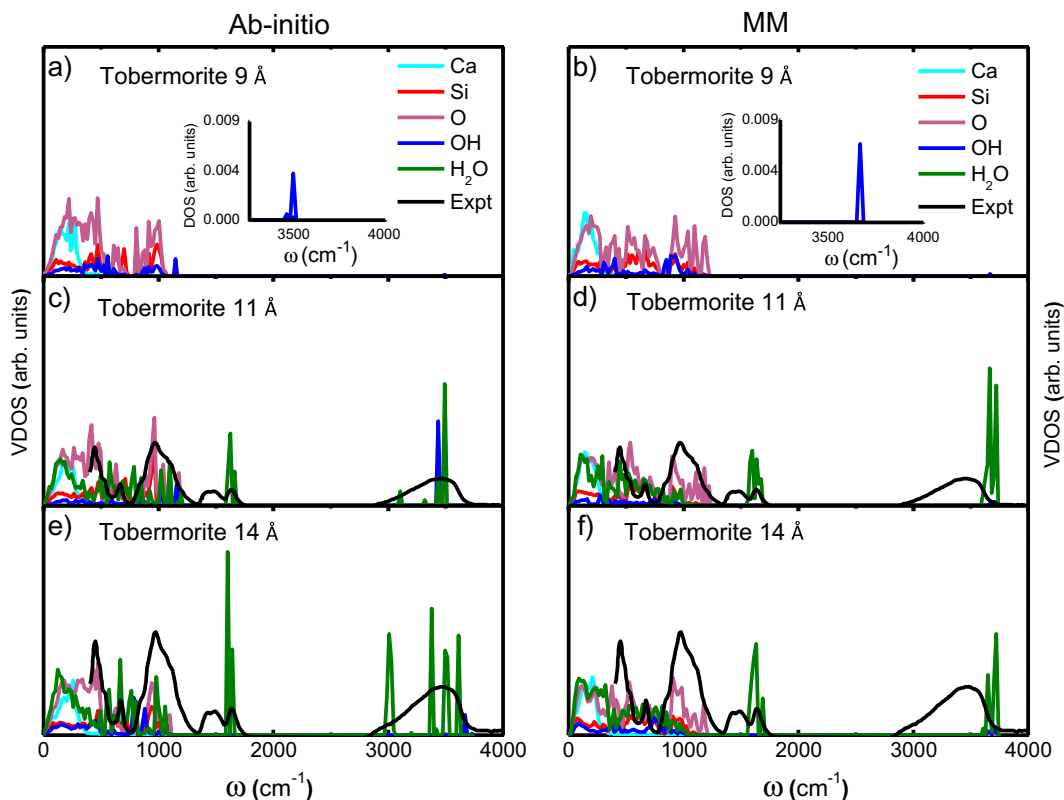
Fig. 4. Partial vibrational density of states of the tobermorite phases calculated from first principles and classical MM approaches. The experimental infrared data is adapted from [75].

our first principles calculations. Classical molecular mechanics simulations for the water vibrations in this range, give similar results to the tobermorite 11 Å structure.

Fig. 5 shows the total vibrational density of states of C_3A, gypsum, and ettringite. The spectrum of C_3A shows a broad band in the ranges 0–1000 cm^{-1}. Projection of the density of states to the constituent atoms (Fig. 6) shows that the Ca—O vibrations are in the 0–450 cm^{-1} range while the Al—O vibrations are present throughout the whole spectrum with major bands at the ranges 450–650 cm^{-1} and 700–900 cm^{-1} for first principles and 700–950 cm^{-1} for classical MM simulations. Infrared spectra of C_3A [78] shows two broad absorption bands in the ranges 650–950 and 380–500 cm^{-1} associated with AlO_4 tetrahedral and AlO_6 octahedral groups respectively which is in good agreement with our findings. The classical MM and first principles approaches agree well in the description of vibrational frequencies of tricalcium aluminate.

For the case of gypsum, the band in the range 0–400 cm^{-1} is mainly due to Ca—O vibrations. The vibrations associated with the antisymmetric bending of the SO_4 tetrahedra show a peak at 518 cm^{-1} for the classical MM and two peaks at 560 cm^{-1} and 635 cm^{-1} for the first principles simulations. The peaks at 1031 cm^{-1} and 1068 cm^{-1} for first principles calculations are associated with the ν_1 symmetric and the ν_3 antisymmetric vibrational stretching modes of the SO_4 tetrahedra respectively [79]. The two stretching modes show up as a single peak at 1274 cm^{-1} for the classical MM simulations. Mid-infrared experiments for gypsum show the SO_4 antisymmetric and symmetric stretching modes at 1102 cm^{-1} and 1003 cm^{-1} respectively and antisymmetric bending modes at 669 and 604 cm^{-1} [78,79]. In the description of the sulfate vibrations, there is a clear distinction between the two methodologies. From these frequencies we can identify two groups of SO_4 tetrahedra from first principles calculations, while for MM calculations, CLAYFF force field shows a highly symmetric sulfate
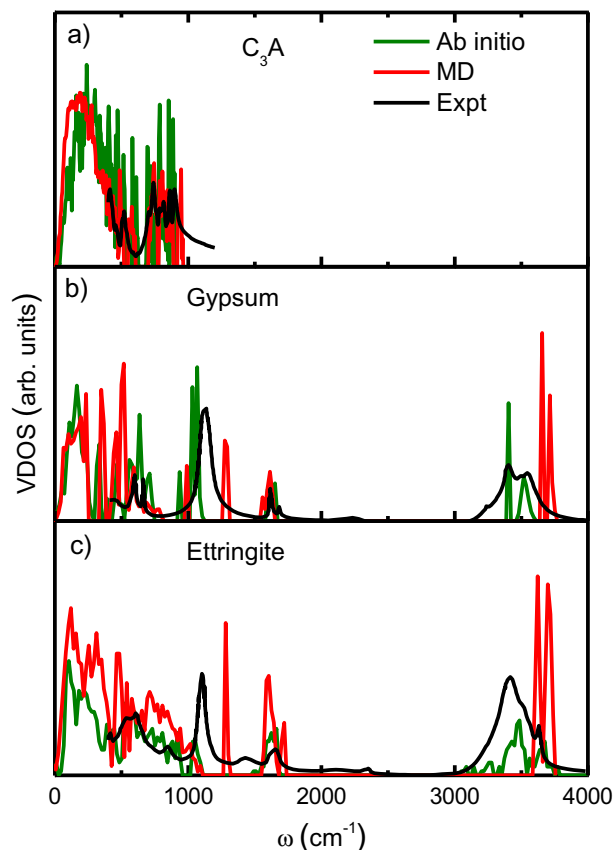
Fig. 5. Total vibrational density of states of C_3A, gypsum and ettringite calculated from first principles and classical MM approaches. The experimental infrared data is adapted from [78].
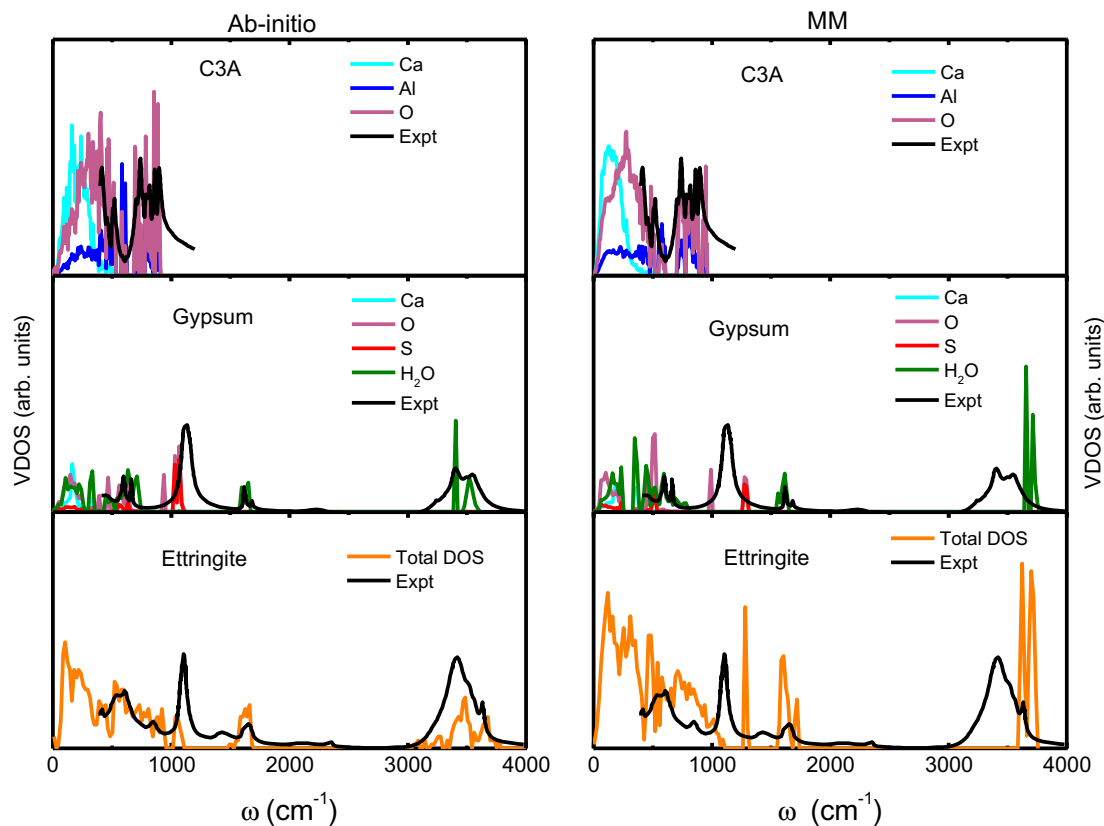
Fig. 6. Partial vibrational density of states of C₃A, gypsum and ettringite calculated from first principles and classical MM approaches. The experimental infrared data is adapted from [78].

group which is attributed to the harmonic bonded interactions of sulfate anion. First principles calculations show a good agreement with experiments for the description of SO_4 tetrahedra vibrations in gypsum.

The water molecule bending modes are characterized by two peaks at 1596 cm^{-1} and 1652 cm^{-1} for first principles and 1558 cm^{-1} and 1614 cm^{-1} for MM. The presence of two peaks indicates crystallographically distinct water molecules. In gypsum, this is associated with water hydrogen bonded to sulfate ions having lower bending modes than calcium coordinated water [80]. The peaks at 3404 cm^{-1} and 3517 cm^{-1} for first principles and 3656 cm^{-1} and 3713 cm^{-1} for classical MM are associated with the symmetric and antisymmetric stretching modes of water respectively.

Ettringite is composed of a mixture of C₃A and gypsum with water, thus, this should be observed in the vibrational spectra. The frequencies in the range $0-1300 \text{ cm}^{-1}$ are dominated by Ca—O, AlO_4, AlO_8 and SO_4 vibrations with the same behavior as described for C₃A and gypsum. The water in ettringite can be grouped into three categories as follows: water in the interchannels, Ca-coordinated water and Al-coordinated OH groups which are shared with calcium atoms [81]. This can be observed in the vibrational spectrum of ettringite by the broad range of stretching modes which varies from 3000 to 3750 cm^{-1}. Our first principles calculations show these variations while the classical MM simulations show only two peaks which is interpreted as the symmetric and antisymmetric stretching water modes. The intensity of the peaks centered at 1650 cm^{-1} which are associated with the bending of H—O—H in water molecules are higher than in gypsum, indicating a higher molecular water content.
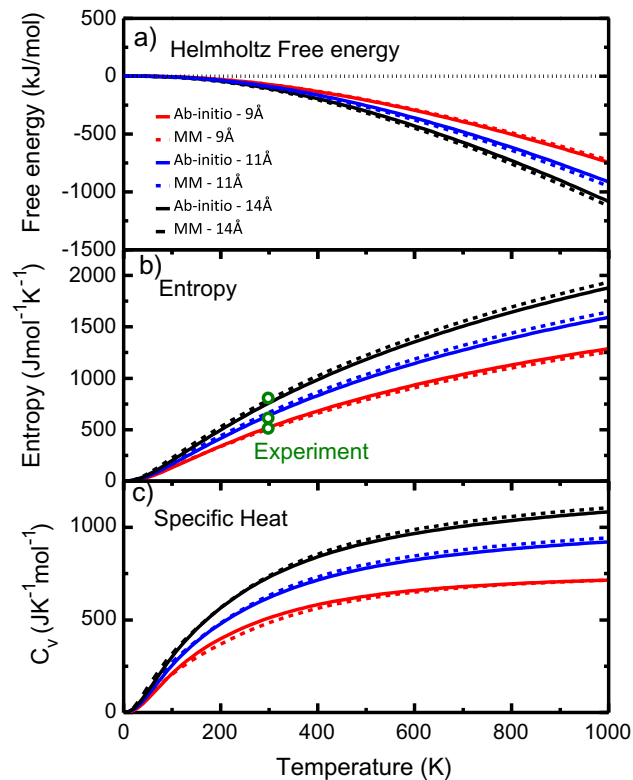
Fig. 7. Thermal properties of tobermorite 9 Å, tobermorite 11 Å and tobermorite 14 Å calculated by both first principles and MM methods. (a) Helmholtz free energy, (b) entropy and (c) specific heat at constant volume. Experimental data for entropy is from [82]. The reference for the Helmholtz free energy is set to the Helmholtz free energy value at 0 K.

3.4. Thermodynamic properties

The thermodynamic quantities determined from the phonon frequencies are shown in Figs. 7 and 8 for tobermorite and ettringite phases respectively. Despite the variation of the frequencies calculated from first principles and MM approaches, there is an overall agreement between both approaches in the prediction of thermal properties.

The variation with respect to hydration on the properties investigated is evident in all the phases. The reference for the Helmholtz free energy is set to the Helmholtz free energy value at 0 K for all the phases. Our results indicate that the hydrated phases are more stable as indicated by the more negative Helmholtz free energy. This implies that water enhances stability of the hydrated phases. The entropy and C_v are least for the anhydrous phases; tobermorite 9 Å, gypsum and C$_3$A. Similar results were obtained for C-S-H with varying degrees of hydration [83].

Experimental entropy data for tobermorite phases at 298 K [82], gypsum from 0 to 320 K [84], C$_3$A from 298 to 1000 K [85,86] and at 298 K for ettringite [87] is in agreement with our first principles and MM simulations (see Figs. 7b) and 8b)). From the determined values of entropy, we estimated the entropy of hydration water based on the hydration reaction taking place from an anhydrous tobermorite 9 Å to hydrated tobermorite 14 Å structure and the formation of ettringite (Eq. (1)). The entropy of hydration water from tobermorite 9 Å to tobermorite 14 Å is 33.4 J/mol/K which is in agreement with the average entropy of hydration water (39.3 ± 4.2 J/mol/K) in silicates [88].

For the ettringite formation, the entropy of hydration water is 35.9 J/mol/K which agrees within experimental error with the value for sulfates (41.5 ± 6.0 J/mol/K) [88]. These values are lower than the liquid water entropy which is 69.9 J/mol/K implying that

the hydration water is ice-like [89]. Our calculations indicate that water in tobermorite 14 Å is more ordered than in ettringite due to its lower entropy. The entropy of hydration water in tobermorite 14 Å and ettringite is similar to that characterizing ice II polymorph which is 41.318 J/mol/K [89].

4. Conclusions

We have compared CLAYFF force field against first principles DFT-GGA calculations for its description of cementitious materials. The systems investigated included both anhydrous phases (C$_3$A and tobermorite 9 Å) and hydrated phases (tobermorite 11 Å, tobermorite 14 Å, gypsum and ettringite). CLAYFF force field describes accurately the lattice parameters, with a slight underestimation for all the hydrated phases. The Si—O bond distances predicted by the CLAYFF force field are short in comparison to both first principles and experimental values. In addition, CLAYFF describes equally all the S—O bond lengths of sulfate anion, failing to capture the two distinct bond distances for sulfate groups in gypsum and ettringite phases as predicted by first principles simulations and experimental data. Bader charge analysis indicate that the charge on the interlayer calcium ions in tobermorite does not change with increase in hydration.

More rigorous investigation of the transferability of CLAYFF force field involved the simulation of the vibrational density of states which depend on the second derivative of energy. We established that CLAYFF force field predicts well Ca—O, Al—O and water bending vibrations in agreement with first principles calculations. However, there is a shift to lower frequencies of the SiO$_4$ deformation vibrational frequencies, which we attribute to the short Si—O bond length. In addition, the SiO$_4$ symmetric/asymmetric stretching vibrations are slightly shifted to higher frequencies. The sym-
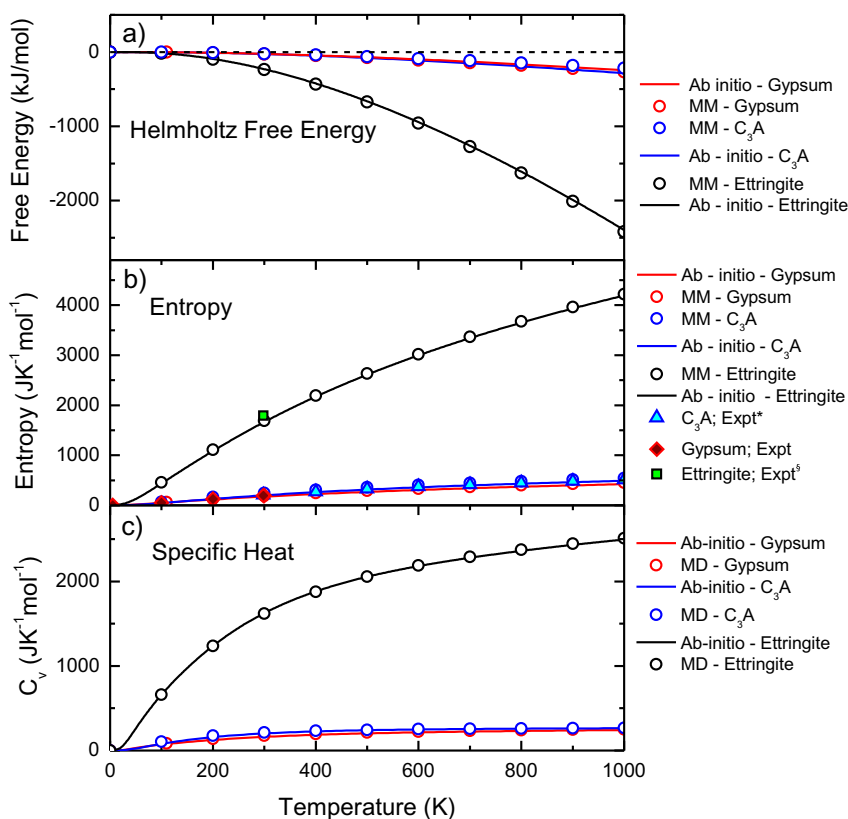
Fig. 8. Thermal properties of gypsum, C$_3$A and ettringite calculated by both first principles and MM methods. (a) Helmholtz free energy, (b) Entropy and (c) Specific heat at constant volume. Experimental data for the entropy are from references; [85,86] for C$_3$A, [84] for gypsum and [87] for ettringite. The reference for the Helmholtz free energy is set to the Helmholtz free energy value at 0 K.

metric/asymmetric stretching modes for water and sulfate from MM simulations are very localized, which is attributed to the bonded harmonic interaction potential. The stretching vibrations for water for all the systems studied here are around $3700 \, cm^{-1}$, which corresponds to weakly hydrogen bonded water, with a $O \cdots O$ distance of about 3.07 Å.

For the description of the thermodynamic properties, there is good agreement between first principles and MM simulations, despite the slight deviations in the frequencies. The entropy of hydration water in both tobermorite 14 Å and ettringite is lower than for liquid water, indicating that it is 'ice–like' and from our simulations, it compares to the ice-II polymorph. Our simulations indicate that CLAYFF force field can capture the thermodynamic properties of the studied cementitious materials within experimental errors.

Acknowledgements

References

[1] R. Kajaste, M. Hurme, Cement industry greenhouse gas emissions–management options and abatement cost, J. Cleaner Prod. 112 (2016) 4041–4052.

[2] B. Cai, J. Wang, J. He, Y. Geng, Evaluating CO_2 emission performance in chinas cement industry: an enterprise perspective, Appl. Energy 166 (2016) 191–200.

[3] S. Komarneni, D. Roy, Mechanisms of immobilization of nuclear waste elements by cement minerals, cement and mortar, Cem. Concr. Res. 11 (5–6) (1981) 789–794.

[4] M. Atkins, F. Glasser, Application of portland cement-based materials to radioactive waste immobilization, Waste Manage. 12 (2) (1992) 105–131.

[5] S. Paria, P.K. Yuet, Solidification-stabilization of organic and inorganic contaminants using portland cement: a literature review, Environ. Rev. 14 (4) (2006) 217–255.

[6] H.F. Taylor, Cement Chemistry, Thomas Telford, 1997.

[7] H. Jennings, B. Dalgleish, P. Pratt, Morphological development of hydrating tricalcium silicate as examined by electron microscopy techniques, J. Am. Ceram. Soc. 64 (10) (1981) 567–572.

[8] L. Aldridge, H. Bordallo, A. Desmedt, Water dynamics in cement pastes, Physica B: Condens. Matter 350 (1) (2004) E565–E568.

[9] H.N. Bordallo, L.P. Aldridge, A. Desmedt, Water dynamics in hardened ordinary portland cement paste or concrete: from quasielastic neutron scattering, J. Phys. Chem. B 110 (36) (2006) 17966–17976.

[10] P. Le, E. Fratini, K. Ito, Z. Wang, E. Mamontov, P. Baglioni, S.-H. Chen, Dynamical behaviors of structural, constrained and free water in calcium-and magnesium-silicate-hydrate gels, J. Colloid Interface Sci. 469 (2016) 157–163.

[11] G. Constantinides, F.-J. Ulm, The nanogranular nature of c–s–h, J. Mech. Phys. Solids 55 (1) (2007) 64–90.

[12] K. Ioannidou, K.J. Krakowiak, M. Bauchy, C.G. Hoover, E. Masoero, S. Yip, F.-J. Ulm, P. Levitz, R.J.-M. Pellenq, E. Del Gado, Mesoscale texture of cement hydrates, Proc. Nat. Acad. Sci. 113 (8) (2016) 2029–2034.

[13] H.M. Jennings, Refinements to colloid model of csh in cement: Cm-ii, Cem. Concr. Res. 38 (3) (2008) 275–289.

[14] H.M. Jennings, A model for the microstructure of calcium silicate hydrate in cement paste, Cem. Concr. Res. 30 (1) (2000) 101–116.

[15] M. Grutzeck, A. Benesi, B. Fanning, Silicon-29 magic angle spinning nuclear magnetic resonance study of calcium silicate hydrates, J. Am. Ceram. Soc. 72 (4) (1989) 665–668.

[16] Y. Okada, H. Ishida, T. Mitsuda, 29si nmr spectroscopy of silicate anions in hydrothermally formed c-s-h, J. Am. Ceram. Soc. 77 (3) (1994) 765–768.

[17] X. Cong, R. Kirkpatrick, 1h–29si cpmas nmr study of the structure of calcium silicate hydrate, Adv. Cem. Res. 7 (27) (1995) 103–111.

[18] E. Roubin, M.A. Shamaa, J.-B. Colliat, A. Pavoine, L. Divet, J.-M. Torrenti, G. Nahas, A nonlinear meso–macro approach to modelling delayed ettringite formation and concrete degradation, Mater. Struct. 47 (11) (2014) 1911–1920.

[19] M. Collepardi, A state-of-the-art review on delayed ettringite attack on concrete, Cem. Concr. Compos. 25 (4) (2003) 401–407.

[20] H. Taylor, C. Famy, K. Scrivener, Delayed ettringite formation, Cem. Concr. Res. 31 (5) (2001) 683–693.

[21] H.-J. Kuzel, Initial hydration reactions and mechanisms of delayed ettringite formation in portland cements, Cem. Concr. Compos. 18 (3) (1996) 195–203.

[22] M. Collepardi, Ettringite formation and sulfate attack on concrete, in: Fifth CANMET/ACI International Conference on Recent Advances in Concrete Technology, SP-200, 2001, pp. 21–38.

[23] J. Stark, K. Bollmann, Laboratory and field examinations of ettringite formation in pavement concrete, in: B. Erlin (Ed.), Ettringite: The Sometimes Host of Destruction, ACI SP-177, 1999, pp. 183–198.

[24] D. Heinz, U. Ludwig, Mechanism of subsequent ettringite formation in mortars and concretes after heat treatment, in: Proceedings of the 8th International Congress on the Chemistry of Cement, Rio de Janeiro, vol. 5, 1986, pp. 189–194.

[25] P. Mehta, Sulfate attack on concrete – a critical review, in: Materials Science of Concrete III, American Ceramic Society, 1992, pp. 105–130.

[26] Rasheeduzzafar, O.S.B. Al-Amoudi, S.N. Abduljauwad, M. Maslehuddin, Magnesium-sodium sulfate attack in plain and blended cements, J. Mater. Civ. Eng. 6 (2) (1994) 201–222.

[27] B. Lothenbach, B. Bary, P. Le Bescop, T. Schmidt, N. Leterrier, Sulfate ingress in portland cement, Cem. Concr. Res. 40 (8) (2010) 1211–1225.

[28] W. Kunther, B. Lothenbach, K.L. Scrivener, On the relevance of volume increase for the length changes of mortar bars in sulfate solutions, Cem. Concr. Res. 46 (2013) 23–29.

[29] R. Shahsavari, R.J.-M. Pellenq, F.-J. Ulm, Empirical force fields for complex hydrated calcio-silicate layered materials, Phys. Chem. Chem. Phys. 13 (3) (2011) 1002–1011.

[30] H. Heinz, T.-J. Lin, R. Kishore Mishra, F.S. Emami, Thermodynamically consistent force fields for the assembly of inorganic, organic, and biological nanostructures: the interface force field, Langmuir 29 (6) (2013) 1754–1765.

[31] L. Liu, A. Jaramillo-Botero, W.A. Goddard III, H. Sun, Development of a reaxff reactive force field for ettringite and study of its mechanical failure modes from reactive dynamics simulations, J. Phys. Chem. A 116 (15) (2012) 3918–3925.

[32] R.T. Cygan, J.-J. Liang, A.G. Kalinichev, Molecular models of hydroxide, oxyhydroxide, and clay phases and the development of a general force field, J. Phys. Chem. B 108 (4) (2004) 1255–1266.

[33] R. Shahriyari, A. Khosravi, A. Ahmadzadeh, Nanoscale simulation of na-montmorillonite hydrate under basin conditions, application of clayff force field in parallel gcmc, Mol. Phys. 111 (20) (2013) 3156–3167.

[34] A. Botan, V. Marry, B. Rotenberg, P. Turq, B. Noetinger, Correction to how electrostatics influences hydrodynamic boundary conditions: poiseuille and electro-osmotic flows in clay nanopores, J. Phys. Chem. C 117 (39) (2013), pp. 20376–20376.

[35] J.A. Greathouse, R.T. Cygan, Molecular dynamics simulation of uranyl (vi) adsorption equilibria onto an external montmorillonite surface, Phys. Chem. Chem. Phys. 7 (20) (2005) 3580–3586.

[36] A. Kalinichev, R. Kirkpatrick, Molecular dynamics simulation of cationic complexation with natural organic matter, Eur. J. Soil Sci. 58 (4) (2007) 909–917.

[37] D. Tavakoli, A. Tarighat, Molecular dynamics study on the mechanical properties of portland cement clinker phases, Comput. Mater. Sci. 119 (2016) 65–73.

[38] D. Lau, Z. Yu, O. Buyukozturk, Mesoscale modeling of cement matrix using the concept of building block, MRS Proceedings, vol. 1759, Cambridge University Press, 2015, pp. 1703–1707.

[39] A.K. Sarkar, M. Barnes, D. Roy, Longevity of borehole and shaft sealing materials: thermodynamic properties of cements and related phases applied to repository sealing, Tech. rep., Pennsylvania State Univ., University Park (USA). Materials Research Lab., 1982.

[40] F.P. Glasser, E.E. Lachowski, D.E. Macphee, Compositional model for calcium silicate hydrate (c-s-h) gels, their solubilities, and free energies of formation, J. Am. Ceram. Soc. 70 (7) (1987) 481–485.

[41] J. Taylor, The heat of formation of xonotlite, tobermorite, hillebrandite and afwillite, in: Conference on the Silicate Industry. Akad Kiado, Budapest, Hungary, 1968, pp. 179–184.

[42] M.J.A. Qomi, F.-J. Ulm, R.J.-M. Pellenq, Physical origins of thermal properties of cement paste, Phys. Rev. Appl. 3 (6) (2015) 064010.

[43] S. Hajilar, B. Shafei, Assessment of structural, thermal, and mechanical properties of portlandite through molecular dynamics simulations, J. Solid State Chem. 244 (2016) 164–174.

[44] T. Honorio, B. Bary, F. Benboudjema, Multiscale estimation of the thermal properties of cement-based materials at early-age, in: Numerical Modeling Strategies for Sustainable Concrete Structures, Rio de Janeiro, Brazil, SSCS, 2015.

[45] P. Hohenberg, W. Kohn, Inhomogeneous electron gas, Phys. Rev. 136 (3B) (1964) B864.

[46] W. Kohn, L.J. Sham, Self-consistent equations including exchange and correlation effects, Phys. Rev. 140 (4A) (1965) A1133.

[47] P.E. Blöchl, Projector augmented-wave method, Phys. Rev. B 50 (24) (1994) 17953–17979.

[48] J.P. Perdew, K. Burke, M. Ernzerhof, Generalized gradient approximation made simple, Phys. Rev. Lett. 77 (18) (1996) 3865–3868.

[49] G. Kresse, J. Hafner, Ab initio molecular dynamics for liquid metals, Phys. Rev. B 47 (1) (1993) 558–561.

[50] G. Kresse, J. Hafner, Ab initio molecular-dynamics simulation of the liquid-metal–amorphous-semiconductor transition in germanium, Phys. Rev. B 49 (20) (1994) 14251–14269.

[51] G. Henkelman, A. Arnaldsson, H. Jónsson, A fast and robust algorithm for bader decomposition of charge density, Comput. Mater. Sci. 36 (3) (2006) 354–360.

[52] S. Plimpton, Fast parallel algorithms for short-range molecular dynamics, J. Comput. Phys. 117 (1) (1995) 1–19.

[53] A.G. Kalinichev, R.J. Kirkpatrick, Molecular dynamics modeling of chloride binding to the surfaces of calcium hydroxide, hydrated calcium aluminate, and calcium silicate phases, Chem. Mater. 14 (8) (2002) 3539–3549.

[54] R.W. Hockney, J.W. Eastwood, Computer Simulation using Particles, CRC Press, 1988.

[55] D.F. Shanno, Conjugate gradient methods with inexact searches, Math. Oper. Res. 3 (3) (1978) 244–256.

[56] A. Togo, I. Tanaka, First principles phonon calculations in materials science, Scripta Mater. 108 (2015) 1–5.

[57] S. Merlino, E. Bonaccorsi, T. Armbruster, Tobermorites: their real structure and order-disorder (od) character, Am. Mineral. 84 (10) (1999) 1613–1621.

[58] S. Merlino, E. Bonaccorsi, T. Armbruster, The real structure of tobermorite 11å normal and anomalous forms, od character and polytypic modifications, Eur. J. Mineral. 13 (3) (2001) 577–590.

[59] E. Bonaccorsi, S. Merlino, A.R. Kampf, The crystal structure of tobermorite 14 å (plombierite), a c–s–h phase, J. Am. Ceram. Soc. 88 (3) (2005) 505–512.

[60] C. Biagioni, E. Bonaccorsi, S. Merlino, D. Bersani, New data on the thermal behavior of 14å tobermorite, Cem. Concr. Res. 49 (2013) 48–54.

[61] A. Dal Corso, A. Pasquarello, A. Baldereschi, R. Car, Generalized-gradient approximations to density-functional theory: a comparative study for atoms and solids, Phys. Rev. B 53 (3) (1996) 1180.

[62] A. Vidmer, G. Sclauzero, A. Pasquarello, Infrared spectra of jennite and tobermorite from first-principles, Cem. Concr. Res. 60 (2014) 11–23.

[63] V.L. Burdick, D.E. Day, Coordination of aluminum ions in tricalcium aluminate, J. Am. Ceram. Soc. 50 (2) (1967) 97–101.

[64] P. Mondal, J. Jeffery, The crystal structure of tricalcium aluminate, ca3al2o6, Acta Crystallogr. Sect. B: Struct. Crystallogr. Crystal Chem. 31 (3) (1975) 689–697.

[65] R.K. Mishra, L. Fernández-Carrasco, R.J. Flatt, H. Heinz, A force field for tricalcium aluminate to characterize surface properties, initial hydration, and organically modified interfaces in atomic resolution, Dalton Trans. 43 (27) (2014) 10602–10616.

[66] P. Comodi, S. Nazzareni, P.F. Zanazzi, S. Speziale, High-pressure behavior of gypsum: a single-crystal X-ray study, Am. Mineral. 93 (10) (2008) 1530–1537.

[67] A. Moore, H. Taylor, Crystal structure of ettringite, Acta Crystallogr. Sect. B: Struct. Crystallogr. Crystal Chem. 26 (4) (1970) 386–393.

[68] M. Hartman, R. Berliner, Investigation of the structure of ettringite by time-of-flight neutron powder diffraction techniques, Cem. Concr. Res. 36 (2) (2006) 364–370.

[69] D. Tunega, A. Zaoui, Understanding of bonding and mechanical characteristics of cementitious mineral tobermorite from first principles, J. Comput. Chem. 32 (2) (2011) 306–314.

[70] S. Hajilar, B. Shafei, Nano-scale investigation of elastic properties of hydrated cement paste constituents using molecular dynamics simulations, Comput. Mater. Sci. 101 (2015) 216–226.

[71] E. Scholtzová, L. Kucková, J. Kožíšek, D. Tunega, Structural and spectroscopic characterization of ettringite mineral–combined dft and experimental study, J. Mol. Struct. 1100 (2015) 215–224.

[72] H. Manzano, J.S. Dolado, A. Ayuela, Structural, mechanical, and reactivity properties of tricalcium aluminate using first-principles calculations, J. Am. Ceram. Soc. 92 (4) (2009) 897–902.

[73] R.K. Mishra, Simulation of interfaces in construction materials: tricalcium silicate, gypsum, and organic modifiers (Ph.D. thesis), The University of Akron, 2012.

[74] R.-M. Pellenq, N. Lequeux, H. Van Damme, Engineering the bonding scheme in c–s–h: The iono-covalent framework, Cem. Concr. Res. 38 (2) (2008) 159–174.

[75] P. Yu, R.J. Kirkpatrick, B. Poe, P.F. McMillan, X. Cong, Structure of calcium silicate hydrate (c-s-h): near-, mid-, and far-infrared spectroscopy, J. Am. Ceram. Soc. 82 (3) (1999) 742–748.

[76] A. Novak, Hydrogen bonding in solids correlation of spectroscopic and crystallographic data, in: Large Molecules, Springer, 1974, pp. 177–216.

[77] S.V. Churakov, Structure of the interlayer in normal 11 å tobermorite from an ab initio study, Eur. J. Mineral. 21 (1) (2009) 261–271.

[78] L. Fernández-Carrasco, D. Torrens-Martín, L. Morales, S. Martínez-Ramírez, Infrared Spectroscopy in the Analysis of Building and Construction Materials, INTECH Open Access Publisher, 2012.

[79] Y. Liu, A. Wang, J. Freemen, Raman, mir, and nir spectroscopic study of calcium sulfates: gypsum, bassanite, and anhydrite, in: Lunar and Planetary Science Conference, vol. 40, 2009, p. 2128.

[80] P.K. Mandal, T.K. Mandal, Anion water in gypsum ($CaSO_4\cdot2H_2O$) and hemihydrate ($CaSO_4\cdot1/2H_2O$), Cem. Concr. Res. 32 (2) (2002) 313–316.

[81] D. Gastaldi, F. Canonico, E. Boccaleri, Ettringite and calcium sulfoaluminate cement: investigation of water content by near-infrared spectroscopy, J. Mater. Sci. 44 (21) (2009) 5788–5794.

[82] L. Clodic, A. Meike, Thermodynamics of calcium silicate hydrates, Development of a Database to Model Concrete Dissolution at 25.

[83] M.A. Qomi, E. Masoero, M. Bauchy, F. Ulm, E. Del Gado, R. Pellenq, Csh across length scales: from nano to micron, in: 10th International Conference on Mechanics and Physics of Creep, Shrinkage, and Durability of Concrete and Concrete Structures, 2015.

[84] R.A. Robie, S. Russell-Robinson, B.S. Hemingway, Heat capacities and entropies from 8 to 1000 k of langbeinite ($K_2Mg_2(SO_4)^3$), anhydrite ($CaSO_4$) and of gypsum ($CaSO_4\cdot2H_2O$), Thermochim. Acta 139 (1989) 67–81.

[85] E. King, Heat capacities at low temperatures and entropies at 298.16 K of crystalline calcium and magnesium aluminates, J. Phys. Chem. 59 (3) (1955) 218–219.

[86] K. Bonnickson, High temperature heat contents of aluminates of calcium and magnesium, J. Phys. Chem. 59 (3) (1955) 220–221.

[87] T. Matschei, B. Lothenbach, F.P. Glasser, Thermodynamic properties of portland cement hydrates in the system $CaO–Al_2O_3–SiO_2–CaSO_4–CaCO_3–H_2O$, Cem. Concr. Res. 37 (10) (2007) 1379–1410.

[88] P. Vieillard, Thermodynamics of Hydration in Minerals: How to Predict these Entities, INTECH Open Access Publisher, 2012.

[89] L. Mercury, P. Vieillard, Y. Tardy, Thermodynamics of ice polymorphs and ice-likewater in hydrates and hydroxides, Appl. Geochem. 16 (2) (2001) 161–181.